




Composite eddy structures on both sides of the Luzon Strait and influence factors

Wen-Zhou Zhang^{1,2,3}  · Qinbiao Ni¹ · Huijie Xue^{4,5}

Received: 30 October 2017 / Accepted: 26 July 2018 / Published online: 9 August 2018
© Springer-Verlag GmbH Germany, part of Springer Nature 2018

Abstract

Combining Argo observations with satellite remote sensing data during the period of 2002–2014, the mean three-dimensional structures of mesoscale eddies on both sides of the Luzon Strait (LS) were obtained via a composite method and analyzed to statistically examine the influences of background marine environment and the Kuroshio current on the eddy structures. The significant signals of temperature and salinity anomalies within the composite eddies extend much deeper in the region east of the LS (zone E) than those in the region west of the strait (zone W) because of stronger eddy intensity and larger vertical gradients of background temperature and salinity in the deep layer in zone E. In the vertical structure of temperature anomaly within the eddies, two cores occur at around 200 and 400 dbar depths, respectively, in zone E and only one core is centered at about 100 dbar in zone W. There is a clear three-core sandwich pattern in the vertical structure of salinity anomaly within the eddies in zone E. The Kuroshio water trapped in the eddy is responsible for abnormally positive salinity anomaly in the surface layer of the anticyclonic eddy center in zone W. On both sides of the LS, an asymmetric dipole structure in the surface layer gradually turns into a monopole one at depths, which resulted from the competition between horizontal advection effect and eddy pumping effect. The Kuroshio current influences the distribution patterns of isotherms and isohalines and enhances background temperature and salinity horizontal gradients on both sides of the LS, determining the orientations of dipole temperature and salinity structures within eddies.

Keywords Mesoscale eddy · Composite structure · Kuroshio current · Luzon Strait

This article is part of the Topical Collection on *the 9th International Workshop on Modeling the Ocean (IWMO), Seoul, Korea, 3–6 July 2017*

Responsible Editor: Sung Yong Kim

✉ Wen-Zhou Zhang
zwenzhou@xmu.edu.cn

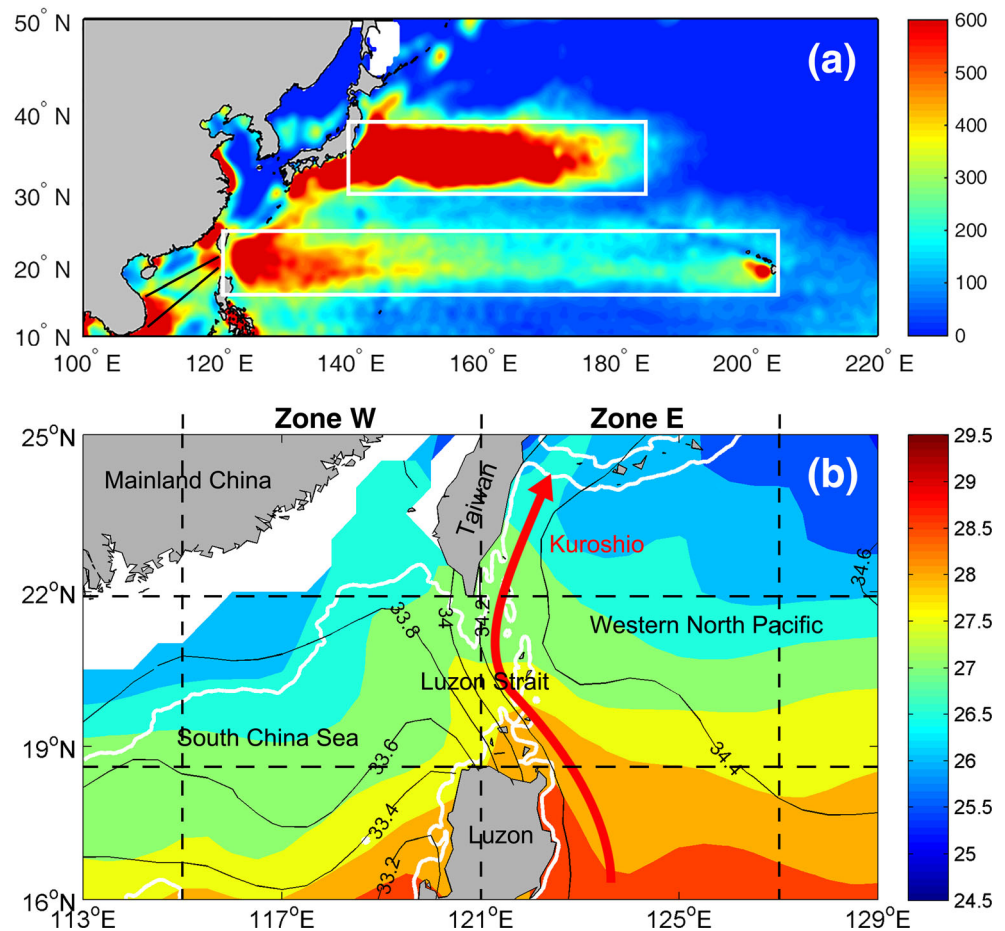
- ¹ Fujian Provincial Key Laboratory for Coastal Ecology and Environmental Studies, Xiamen University, Xiamen, China
- ² State Key Laboratory of Satellite Ocean Environment Dynamics, Second Institute of Oceanography, SOA, Hangzhou, China
- ³ Department of Physical Oceanography, College of Ocean and Earth Sciences, Xiamen University, Xiamen 361005, Fujian, China
- ⁴ State Key Laboratory of Tropical Oceanography, South China Sea Institute of Oceanology, CAS, Guangzhou, China
- ⁵ School of Marine Sciences, University of Maine, Orono, ME, USA

1 Introduction

Located between Taiwan Island and Luzon Island, the Luzon Strait (LS) is a very short, broad, and deep strait, connecting the South China Sea (SCS) with the western North Pacific (WNP; Fig. 1). The Kuroshio current, the most important west boundary current in the North Pacific, flows northward beside the LS and the Kuroshio water with high temperature and salinity frequently intrudes into the SCS via the LS (Hu et al. 2000; Caruso et al. 2006; Nan et al. 2015). Energetic mesoscale eddies, including cyclonic eddies (CEs) and anticyclonic eddies (AEs), are ubiquitous on both sides of the LS (e.g., Wang et al. 2003; Chen et al. 2011; Liu et al. 2012; Yang et al. 2013).

Two zonal bands with abundant eddies have been found in the North Pacific Ocean (Fig. 1a): the Kuroshio Extension (northern band) and the subtropical area (southern band) (Aoki and Imawaki 1996; Liu et al. 2012). The LS is just located near the west end of the southern band. In the subtropical WNP, eddies usually propagate westward (Roemmich and Gilson 2001; Liu et al. 2012; Yang et al. 2013), some of which can reach the

Fig. 1 **a** Two zonal bands with abundant eddies in the North Pacific (marked by two white rectangles) and two bands of significant mesoscale variability in the South China Sea (SCS) (marked by two black lines). The shading colors denote time-averaged eddy kinetic energy (EKE, cm^2/s^2) during the period of interest. **b** Temperature (shading, $^{\circ}\text{C}$) and salinity (contour, psu) fields in the vicinity of the Luzon Strait (LS) averaged from the surface to 100-m depth, based on the Commonwealth Scientific and Industrial Research Organization (CSIRO)'s Atlas of Regional Seas (CARS) climatology. White curves represent the 1000 m isobath. Zone W denotes the region (115° – 121° E, 16° – 25° N) west of the LS and zone E the region (121° – 127° E, 16° – 25° N) east of the LS



Kuroshio before they disappear. The occurrence frequency of eddies in the South China Sea observed by satellite altimetry is very high in the subtropical band of 19° – 26° N, especially near the west boundary from Luzon Island to Taiwan Island (Yang et al. 2013). Eddies can drive local thermocline and halocline upward or downward, inducing temperature and salinity anomalies within the eddies (Liu et al. 2012). Liu et al. (2012) examined eddy effects on the thermocline and halocline in the southern band. They found that CE (AE) induce a negative (positive) maximum temperature anomaly at 150 m depth and the eddy impact on temperature can reach about 1000 m depth, and meanwhile, they displace the depth of maximum salinity upward (downward). Yang et al. (2013) demonstrated that in the subtropical WNP, a double-core vertical structure appears in the eddy-induced temperature anomaly due to the existence of mode waters in the main thermocline and a sandwich-like pattern occurs in the eddy-induced salinity anomaly.

In the SCS, there are two narrow bands of significant mesoscale variability (Fig. 1a): one is along the northern and western continental slopes, and the other extends southwestward from the LS to the Vietnam coast (Wang et al. 2000, 2003). Both bands originate from the northeastern SCS, and the flows associated with the Kuroshio intrusion in the LS support the development

and maintenance of their mesoscale variability (Wang et al. 2000). Mesoscale eddies in the SCS are usually generated by the instability of the Kuroshio intrusion and local wind forcing under the Asian monsoon system (Wang et al. 2003, 2008; Jia and Chassignet 2011). Many studies have been conducted on the activity of mesoscale eddies in the SCS based on the satellite altimetry data, satellite-tracked surface drifter data, and numerical simulations (e.g., Wang et al. 2003; Xiu et al. 2010; Li et al. 2011). Recently, a few statistical and case analyses focus on the three-dimensional (3D) structures and evolution of eddies using Argo profiles, moored data, field survey data, or model results (e.g., Chu et al. 2014; Lin et al. 2015; Zhang et al. 2015, 2016).

Although two regions on both sides of the LS are abundant of eddies, all studies mentioned above separately paid attention on the eddies in the subtropical WNP or in the SCS and none of them synchronously analyzed and compared 3D structures of eddies in the two regions. These two regions are very close and adjacent to each other via the LS. However, the eddies in the two regions must have different structures since they are separated by the Kuroshio current flowing northward across the LS (Fig. 1b). What are the main differences in the eddy structures between the two regions? What factors affect the structures of the eddies in these two

adjacent regions? These questions are still unanswered in the literature. Thus, we obtained the 3D structures of composite eddies in the two regions and analyzed their differences in attempt to examine the influences of both background marine environment and the Kuroshio current on the eddy structures on the two sides of the LS. For simplicity, the area west of the LS (115°–121° E, 16°–25° N) is referred to as zone W and the area east of the strait (121°–127° E, 16°–25° N) as zone E (Fig. 1b), ignoring the short length of the LS itself. Their region size was determined from the competition between containing enough available Argo profiles and keeping the influence of the Kuroshio perceptible via a few cut-and-try experiments. Zone W is constrained by mainland China to the northwest, and zone E is open ocean with abruptly changing bathymetry and persistent Kuroshio regional current.

2 Data and methods

2.1 Data

The daily sea level anomaly (SLA) data used in this work were provided by the Archiving, Validation, and Interpretation of Satellite Oceanographic (AVISO) data project (<ftp://ftp.aviso.oceanobs.com>). They have been applied in detecting and tracking mesoscale eddies. The daily satellite Advanced Very High Resolution Radiometer (AVHRR) infrared sea surface temperature (SST) data were obtained from the National Climatic Data Center (NCDC) of the National Oceanic and Atmospheric Administration (NOAA). Both datasets have a spatial resolution of 0.25°.

The Argo float profiles downloaded from the China Argo Real-time Data Center were used to construct the 3D structures of eddies. These profiles have undergone quality control by the center staff. Only the profiles with pressure (*P*), temperature (*T*), and salinity (*S*) records with a flag of 1 (for good quality) were selected. Following Chaigneau et al. (2011), the selected profiles should also satisfy three criteria as follows. (1) The smallest value of *P* (shallowest depth) is < 10 dbar and the biggest (deepest) is > 1000 dbar. (2) The differences of *P* between two adjacent levels are ≤ 25 dbar for 0–100 dbar, ≤ 50 dbar for 100–300 dbar, and ≤ 110 dbar for 300–1000 dbar. The last threshold is slightly larger than 100 dbar adopted by Chaigneau et al. (2011), allowing more usable profiles (4477 vs. 2636). (3) There are at least 30 observation levels in the profile above 1000 dbar.

To depict the eddy structures, anomalies were calculated by removing the climatological counterparts from Argo profiles (Chaigneau et al. 2011; Souza et al. 2011a; Wang et al. 2012). The Commonwealth Scientific and Industrial Research Organization (CSIRO)’s Atlas of Regional Seas (CARS) climatology mapped onto a 0.5° × 0.5° grid was used as the climatological counterparts in the present study. Yang et al. (2013) remarked that this product performs better in the

western boundary region compared with other climatological products. All the abovementioned data were extracted for the period from 2002 to 2014.

2.2 Eddy detection and tracking method

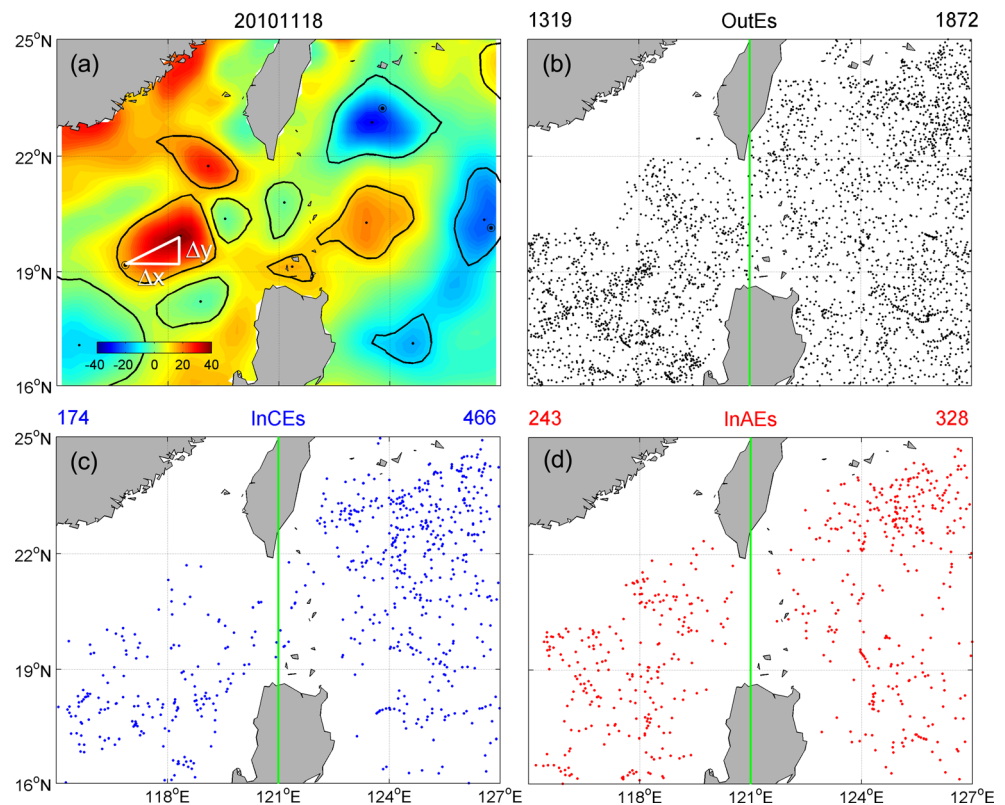
The eddy detection method was modified from two similar methods presented by Chaigneau et al. (2009) and Chelton et al. (2011). These SLA contour-based methods have great advantages over the commonly used Okubo–Weiss method in terms of correctness and accuracy (Souza et al. 2011b). Contours with an interval of 0.5 cm were plotted in SLA maps. For each eddy, the geometric center of its innermost enclosed contour is regarded as its center and the outmost enclosed contour as its edge. Once the center and edge of an eddy are identified, its parameters (amplitude, type, and radius) can be computed. Following Chaigneau et al. (2011), if the amplitude of an eddy is less than 2 cm (altimeter observation error), then the eddy is abandoned. As an example, a snapshot of eddy detection result near the LS on 18 November 2010 is presented in Fig. 2a.

According to the geostrophic balance, the sea surface geostrophic velocity anomaly $\mathbf{V}'_s(u'_s, v'_s)$, eddy kinetic energy ($EKE = \frac{1}{2}u'^2_s + \frac{1}{2}v'^2_s$), and vorticity ($VOR = \frac{\partial v'_s}{\partial x} - \frac{\partial u'_s}{\partial y}$) are derived from the SLA maps (Chaigneau et al. 2009). The eddy trajectories are tracked using a similar parameter (S_{e_1, e_2}) to that adopted by Chaigneau et al. (2009). Suppose that eddy e_1 is detected at time step t_1 and eddy e_2 detected at t_2 , the similarity of eddy e_1 and eddy e_2 can be calculated as follows:

$$S_{e_1, e_2} = \sqrt{\left(\frac{\Delta D}{50}\right)^2 + \left(\frac{\Delta R}{10}\right)^2 + \left(\frac{\Delta EKE}{10}\right)^2 + \left(\frac{\Delta VOR}{1.3 \times 10^{-6}}\right)^2},$$

where ΔD , ΔR , ΔEKE , and ΔVOR are the distance and the differences in eddy radius, EKE, and VOR, respectively, between e_1 and e_2 . The eddy pair (e_1, e_2) with the minimum S_{e_1, e_2} is taken as the same eddy at the two successive time steps. A searching length or searching radius (*L*) is required to be prescribed beforehand. Ideally, the searching length should cover the maximum moving distance of eddies from one time step to the next time step in order to avoid artificially splitting a continuous track for a single eddy into two tracks for two different eddies. The eddy moving distance between two consecutive time steps (t_1, t_2) mostly depends on both the time resolution ($\Delta t = t_2 - t_1$) of dataset and the current speed of background flow field since eddies are advected by local currents (Nencioli et al. 2010). In practice, the searching length can be estimated by the product of the mean flow speed and the time resolution (Nencioli et al. 2010). So we chose a searching length which is slightly greater than the product of the mean flow speed and the time resolution. Taking the spatial resolution of SLA data into account, it was set to be 30 km

Fig. 2 **a** A snapshot of sea level anomaly (SLA) field with identified eddies near the LS on November 18, 2010, as an example, and distribution of the Argo profiles (dots) located **b** outside of eddies (OutEs), **c** inside cyclonic eddies (InCEs), and **d** inside anti-cyclonic eddies (InAEs) during the period of 2002–2014. The Δx and Δy in **a** denote the zonal and meridional distances, respectively, from eddy center (dot) to an Argo profile in an eddy. The green line at 121° E longitude divides the study area into two subdomains: zone W and zone E as shown in Fig. 1b. In the **b–d**, the number of profiles in each zone is presented above each panel



for the mean flow speed of 0.2–0.3 m/s and time resolution of 1 day in this work. An eddy may disappear in one of consecutive SLA maps if it passes into a gap between satellite ground tracks, or it may not be detected due to errors associated with the eddy identifying method (Chaigneau et al. 2008; Nencioli et al. 2010). To reduce this problem, we search for the same eddy with an increased searching length (1.5 L) in the map at the time step $t + 2$ if it is not be detected at the time step $t + 1$, following Nencioli et al. (2010). In this work, the trajectories with lifespan shorter than 20 days were discarded.

2.3 Composite method of eddy structure

Using the Akima interpolation (Akima 1970), the Argo T/S profiles were separately interpolated onto 100 vertical levels from 10 to 1000 dbar with the interval of 10 dbar. The Akima interpolation is based on a piecewise function composed of a set of locally determined polynomials with a degree of no more than three (Akima 1970). The curve resulted from this interpolation method looks smooth and natural, compared with the resultant curve of the commonly used linear interpolation. Assume that the seawater at 1000 dbar level be stationary, the dynamical height (H) at each vertical level can be calculated from T and S (Chaigneau et al. 2011). Then, the potential temperature anomaly (θ'), salinity anomaly (S') and dynamical height anomaly (H') were obtained by subtracting the corresponding climatological profiles from the Argo

profiles. The geostrophic current anomaly $\mathbf{V}'(u', v')$ was derived from the H' slope:

$$u' = -\frac{g}{f} \frac{\partial H'}{\partial y},$$

$$v' = \frac{g}{f} \frac{\partial H'}{\partial x},$$

$$V' = |\mathbf{V}'| = \sqrt{u'^2 + v'^2},$$

where u' and v' are the zonal and meridional components of \mathbf{V}' , respectively. f is the Coriolis parameter at the central latitude of the study area. At the surface, θ' was obtained by subtracting the CARS climatology from the SST, and \mathbf{V}' , namely \mathbf{V}'_s , was calculated from SLA slope. There is no surface S' because of lack of available salinity data at the surface.

According to the locations of Argo profiles relative to the eddies, the profiles were classified into three types (Chaigneau et al. 2011): inside the CEs (InCEs), inside the AEs (InAEs), and outside eddies (OutEs). The numbers of the three-type profiles in zone E (zone W) are 466, 328, and 1872 (174, 243, and 1319), respectively, as shown in Fig. 2. Although the profiles in zone W are less than their counterparts in zone E, they are enough to reveal the general structures of the CEs and AEs. The first two types of Argo profiles were further transformed into an eddy coordinate system (one example shown in Fig. 2a). In this system, Δx and Δy are the latitudinal and meridional distances, respectively, from an eddy center to

the position of an Argo profile. To eliminate the impact of eddy radius on the composite results, both Δx and Δy were normalized, that is, divided by the eddy radius R .

Finally, at each vertical level, anomalies larger than three times the interquartile range from either the first or third quartiles were removed (Chaigneau et al. 2011). The remaining data were objectively mapped onto a 0.1×0.1 grid using the variational interpolation (Barth et al. 2014). To optimize the outcome, two parameters should be set beforehand. The spatial correlation length was set to 1, corresponding to eddy radius, following Chaigneau et al. (2011). This value can not only filter out small-scale variability but also ensure enough data for the interpolation (Chaigneau et al. 2011). The signal-to-noise ratio was set to 0.3 for H' and 0.2 for the other two anomalies to minimize the root-mean-square difference between observations and corresponding interpolation results, based on a statistical way which is described detailedly in the website related to the variational interpolation (<http://modb.oce.ulg.ac.be/mediawiki/index.php/Divand>).

In a day, there is usually only an Argo profile within a real eddy. It is impossible to calculate geostrophic current with such single profile. In the normalized coordinates, we calculated composite \mathbf{V}' structure directly from composite H' structure for consistency. To do so, the slope of H' was estimated by the following formula,

$$\frac{\partial H'}{\partial r} \approx \frac{\partial H'}{R \partial r_n},$$

where r is the distance to eddy center, r_n the normalized distance to composite eddy center, and R the averaged eddy radius. This method may cause some error due to different radius for individual eddies. However, the resultant composite \mathbf{V}' structure is compatible with the composite H' structure and then corresponding θ' and S' structures, and it is acceptable since all composite structures are statistically average.

The composite method has been successfully used to obtain the general structures of eddies in the literature (e.g., Roemmich and Gilson 2001; Chaigneau et al. 2011; Yang et al. 2013; Zhang et al. 2013). Applying this method to XBT transects and altimeter data, Roemmich and Gilson (2001) investigated the composite structures of mesoscale eddies in the North Pacific Ocean. A large number of Argo profiling data have been obtained in open oceans since 1999. Combining these Argo data with satellite altimetry, Chaigneau et al. (2011) constructed the mean 3D eddy structures in the eastern South Pacific Ocean via the composite method. Following them, Yang et al. (2013) obtained the composite eddies in the subtropical WNP. Zhang et al. (2013) constructed a common 3D structure in normalized stretched coordinates for mesoscale eddies in global oceans. Recently, similar studies were separately conducted in the Kuroshio extension region and the SCS by Sun et al. (2017, 2018).

3 Results and discussion

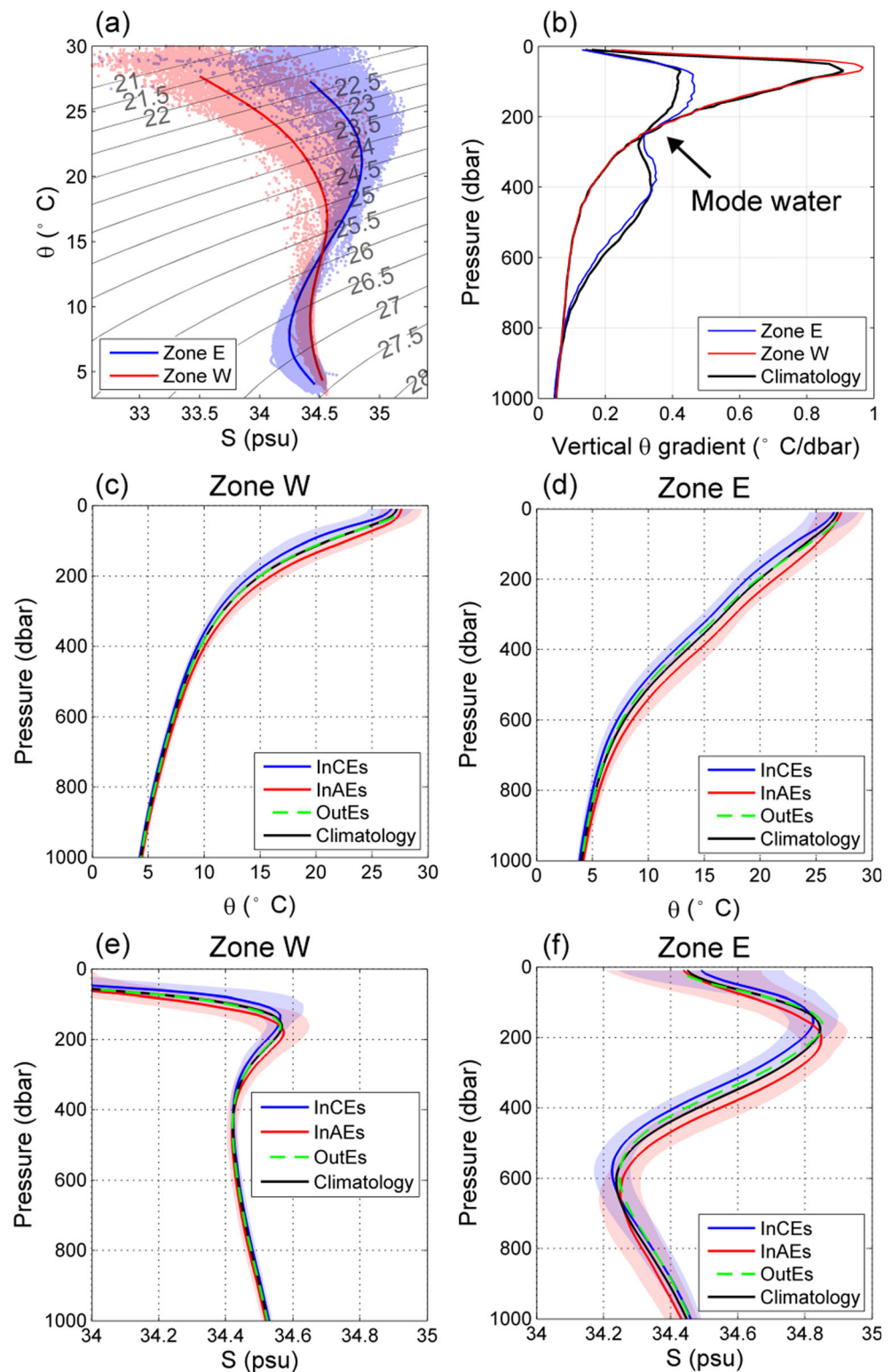
3.1 Vertical structure of eddy

Figure 3a shows the θ – S diagrams of water masses in the two zones, based on the observations outside of eddies. In an isopycnal surface, the water in zone E, on average, has higher temperature and salinity than that in zone W above the layer of 25.8 kg/m^3 (minus 1000 kg/m^3) while it is just the opposite below (Fig. 3a). In zone E, the water is obviously warmer above 700 dbar but slightly cooler in the layer of 700–1000 dbar, compared with the water in zone W (Fig. 3c, d). For salinity, the transition depth is near 400 dbar, above (below) which it is higher in zone E (zone W). Qu et al. (2000) documented that “at any given depth in the upper thermocline the Pacific water is warmer and saltier than the SCS water.” Obviously, the transition depths for temperature (700 dbar) and for salinity (400 dbar) are definitely different in the present results. In the upper 200 dbar except the mixed layer, both temperature and salinity of the SCS water in zone W change more sharply with depth than their counterparts of the Pacific water in zone E (Fig. 3b–f). In the deep layer (200–800 dbar), the case is reverse. The influence of the Pacific water on the SCS water decreases from northeast (near the LS) to southwest (Qu et al. 2000). Although both zones E and W are adjacent to the LS, their water masses have much difference, seen from the above results.

Figure 3b shows that in zone E there is a prominent trough of temperature vertical gradient in 200–400 dbar, which is not found in zone W. This weak temperature gradient layer indicates the existence of the North Pacific Subtropical Mode Water (STMW) locally formed in the deep convective mixed layer and widely distributed by lateral advection (Suga and Hanawa 1995). The STMW splits the main thermocline into two vertical portions (Yang et al. 2013), as distinctly shown in Fig. 3b.

Figures 4 and 5 show a prominent difference in vertical structures of temperature, salinity, and geostrophic velocity anomalies between eddies in zone E and eddies in zone W, that is, the strong signals of eddies extend much deeper in zone E than their counterparts in zone W. In the composite CE, the obvious negative temperature anomaly (at least $-0.45 \text{ }^\circ\text{C}$) caused by the combination of eddy-induced upwelling and temperature decreasing with depth reaches deeper than 750 dbar in zone E (Fig. 4b) while it only appears above the 300 dbar in zone W (Fig. 4a). The depth of significant salinity anomaly with a magnitude larger than 0.04 psu in zone E (larger than 500 dbar) is five times that in zone W (about 100 dbar). As shown in Fig. 4e, f, eddy-induced velocity anomaly affects deeper water in zone E, compared to zone W. Similar results also appear in the composite AE (Fig. 5) except that the signs of the anomalies are generally opposite to those of their counterparts in the composite CE. The

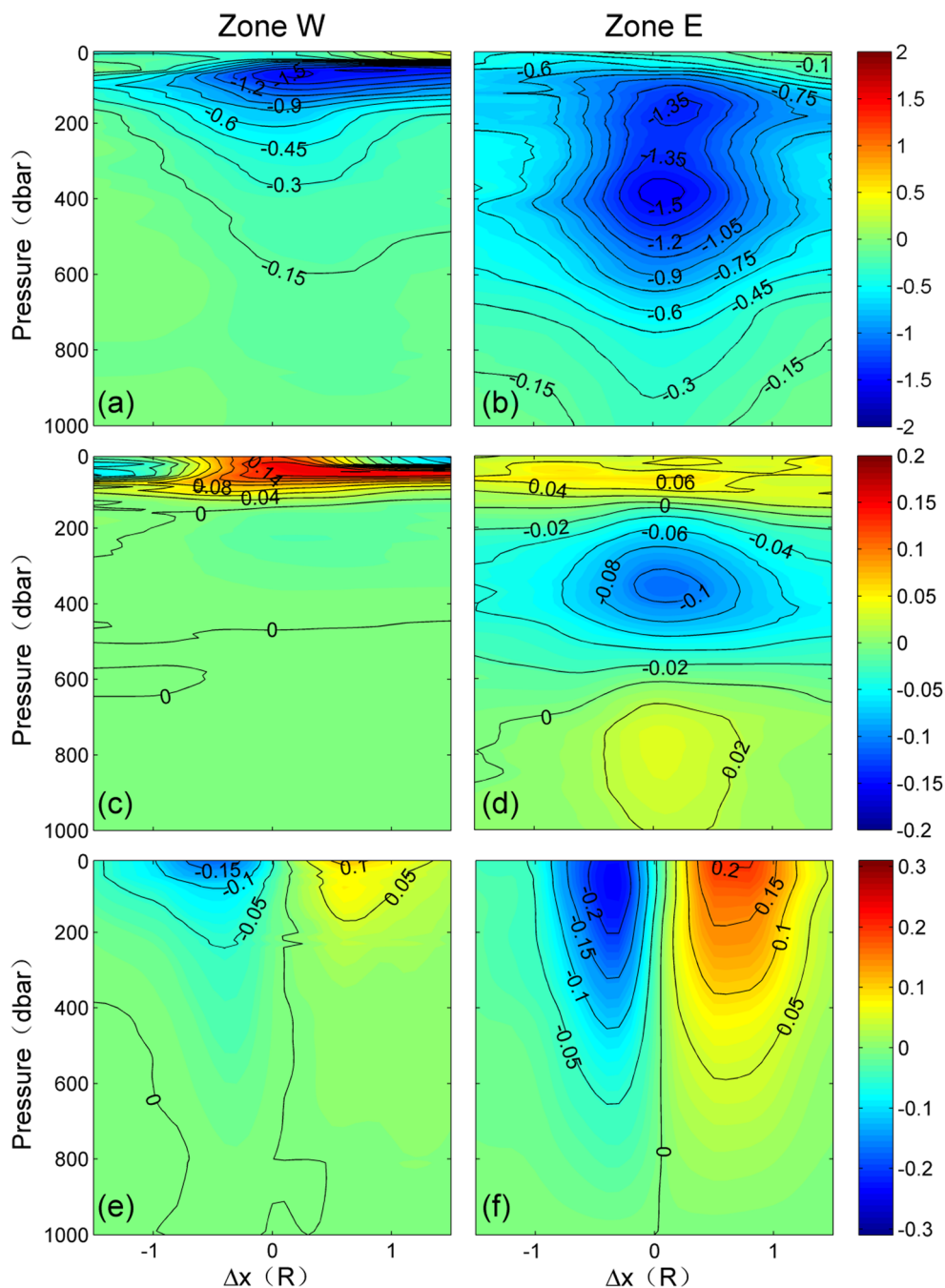
Fig. 3 **a** Potential temperature (θ)-salinity (S) diagram. Dots denote Argo observations obtained outside of eddies. Blue and red curves mark the mean values in zone E and zone W, respectively. **b** Mean vertical profiles of the θ gradient obtained from the OutEs temperature profiles and from climatological data, describing the background of the θ gradient. Mean temperature profiles in zones **c** W and **d** E and mean salinity profiles in zones **e** W and **f** E, obtained from Argo observations and from climatological data. The results obtained from the Argo profiles outside of eddies are in good agreement with those from climatological data in **b–f**



difference in the depth of temperature or salinity anomaly between zone E and zone W is very clear in mean profiles within the core area of the eddies (Fig. 6), too. The deepest depth for large temperature anomaly (≥ 1 °C) is near 600 dbar in zone E, but less than 200 dbar in zone W. For large salinity

anomaly (≥ 0.05 psu), its deepest depth is approximately 500 (100) dbar in zone E (W). Previous studies showed that eddy-induced temperature anomaly larger than 0.4 °C can reach 800 dbar in the region just east of the LS (Yang et al. 2013) while it exists only in the upper 300 m (dbar) in the SCS (Chen

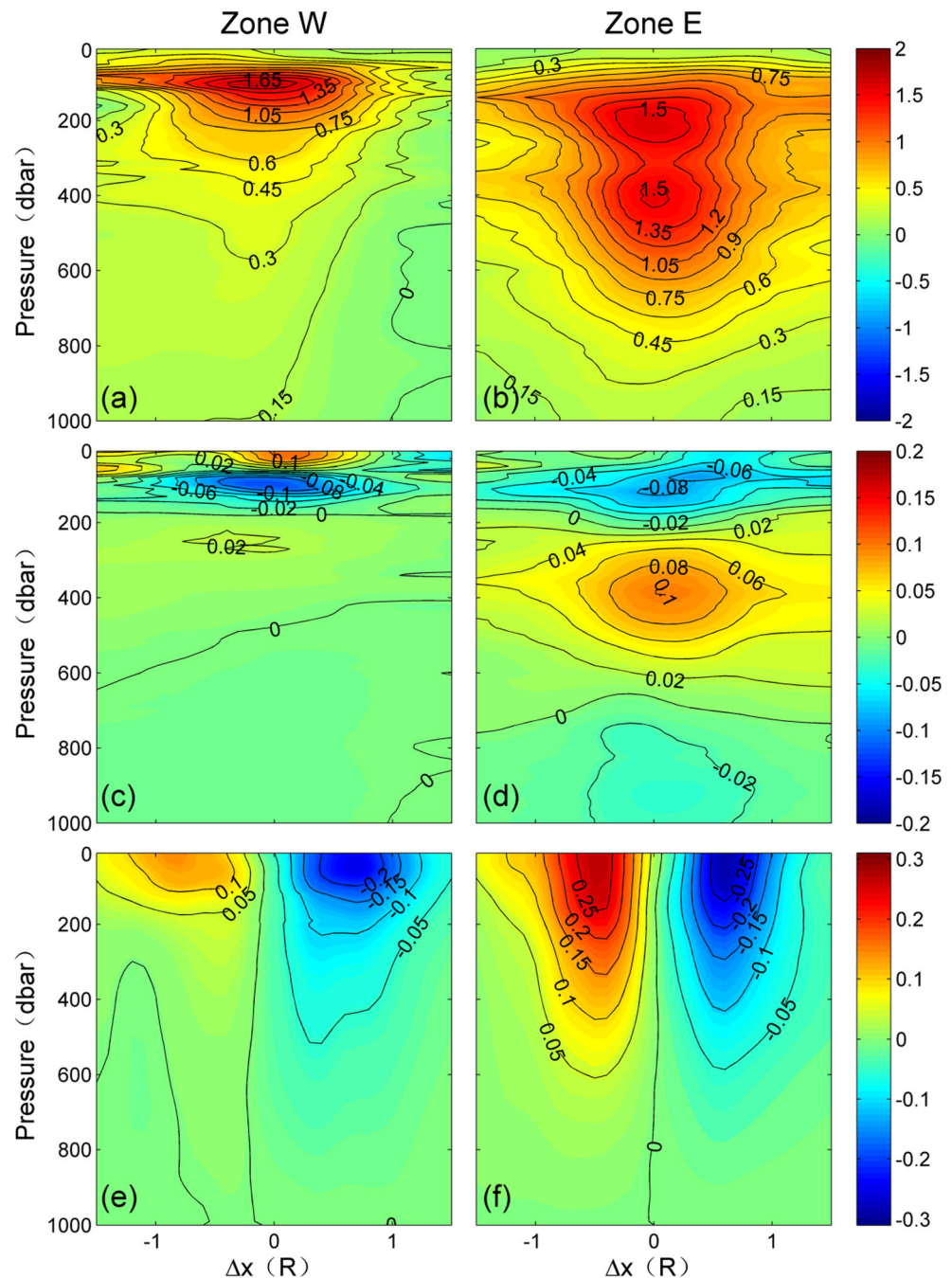
Fig. 4 Zonal sections of the potential temperature anomaly θ' ($^{\circ}\text{C}$, top), salinity anomaly S' (psu, middle) and meridional geostrophic current anomaly v' (m/s, bottom) at $\Delta y = 0$ in the normalized coordinate system of the composite CE for each zone



et al. 2011). Two factors may be responsible for such difference in the influence depth of eddies between zone E and zone W. One is that the vertical gradients of temperature and salinity in zone E are larger than those in zone W in the deep layer of 200–800 dbar, which are seen in Fig. 3b, e, f. For a given eddy-induced vertical motion with the same action time, a greater temperature/salinity anomaly will be generated in the sea area with a larger vertical temperature/salinity gradient. The other is that the eddies in zone E tend to be stronger. Temperature and salinity profiles can be shifted upward (downward) by prevailing upwelling (downwelling) in the

CEs (AEs) with respect to profiles outside of eddies or climatological profiles (Fig. 3c–f). The vertical displacements of temperature and salinity profiles in eddies are slightly larger in zone E than those in zone W. A comparison of Figs. 4e–f and 5e–f indicates that the circular currents in eddies are obviously stronger and extend deeper in zone E. Obtained from independent altimeter SLA data, the eddies east of the LS, on average, have larger radius and amplitude, longer lifespan, and travelling distance (see Table 1), compared with those west of the LS. All these demonstrate a stronger composite eddy in zone E than that in zone W.

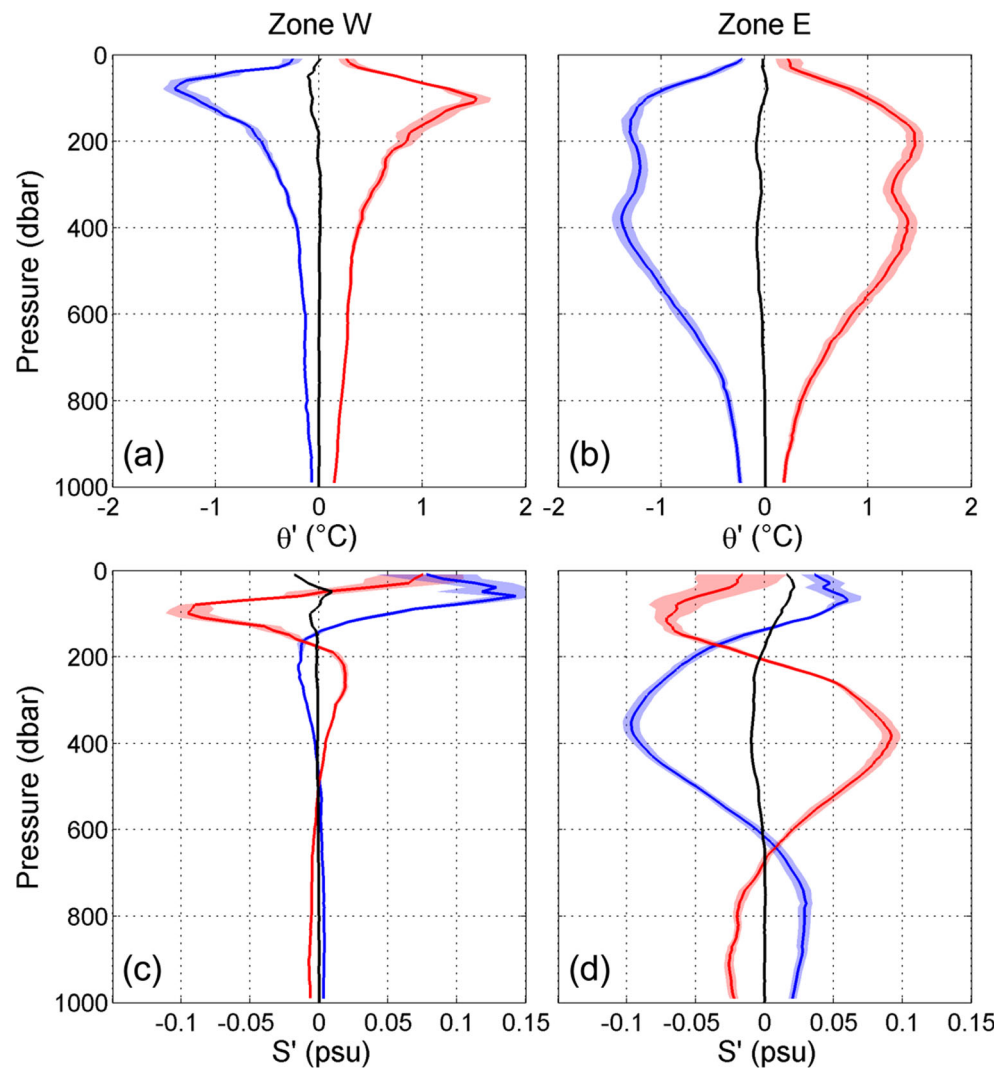
Fig. 5 Same as Fig. 4, but for the composite AE



Another significant difference exists in the patterns of temperature and salinity anomalies. For the temperature anomaly, there are two cores located near the depths of 200 and 400 dbar, respectively, in both composite CE and AE of zone E (Figs. 4b and 5b) while only one core occurs at around 100 dbar in the eddies of zone W (Figs. 4a and 5a). These cores correspond to the peaks or troughs of mean profiles shown in Fig. 6a, b. The locations of the two cores coincide with the depths of vertical temperature gradient peaks in zone E (Fig. 3b), indicating their cause—the STMW. The STMW with weak temperature gradient divides the main thermocline

with strong temperature gradient into upper and lower parts (Yang et al. 2013; Fig. 3b) which are corresponding to the two negative (positive) temperature anomaly cores induced by upwelling (downwelling) in the CE (AE). These are consistent with the results in the subtropical WNP presented by Yang et al. (2013) who found a double-core vertical structure in the eddy-induced temperature anomaly with two cores in the upper 200 dbar and in the layer of 300–700 dbar, respectively. Since there is no STMW in the SCS, only one temperature anomaly core can be formed in the thermocline in zone W by upwelling/downwelling in the eddies. Sun et al. (2018) also

Fig. 6 Mean profiles of θ' (top) and S' (bottom) within the composite CE (blue) and AE (red) for each zone. Each mean profile is obtained by horizontally averaging all Argo profiles inside the core area (defined by the local maximum geostrophic velocity around the eddy) of the corresponding composite eddy. Shading denotes the range from mean profile to one corresponding standard deviation. The black curve in each panel shows the mean profile outside of eddies



showed that in the SCS, eddy-induced temperature anomaly increases with depth until reaching its maximum and then decreases with depth; the maximum anomaly appeared at about 70 m (100 m) in the composite CE (AE) obtained from Argo observations.

Table 1 Statistical characteristics of eddies with a lifespan ≥ 20 days on both sides of the LS, based on the altimeter SLA data

	Zone W		Zone E	
	CE	AE	CE	AE
Number	166	162	289	257
Radius (km)	83.7	91.2	103.4	105.7
Amplitude (cm)	-7.4	9.2	-13.1	11.0
Lifespan (days)	36.6	41.2	49.0	43.6
Distance (km)	256.2	293.4	415.4	370.0
Travelling speed (cm/s)	8.2	8.1	10.3	10.2

For the salinity anomaly, upwelling/downwelling in cyclonic/anticyclonic eddies can produce a three-core sandwich pattern (positive–negative–positive/negative–positive–negative) due to the inverse S structure of salinity profile. This pattern is very clear in the salinity anomaly induced by eddies in zone E (Figs. 4d and 5d) where the inverse S structure of salinity profile is prominent (Fig. 3f). The interfaces between the three cores are consistent in depth with the peak (near 200 dbar) and trough (600 dbar) of salinity profile, which can be identified in Figs. 3d, 4d, and 5d. The salinity vertical gradient at the peak and trough are the weakest and thus vertical motion produces a small salinity anomaly there. In Yang et al. (2013), a similar sandwich-like pattern in the eddy-induced salinity anomaly was also found within the AE in the far western Pacific but absent within the CE primarily due to its weaker strength. In zone W, the inverse S structure of salinity profile is not so distinct as that in zone E, particular in the deep layer below 300 dbar. More importantly, the strength of eddies is weaker and the influence depth is

shallower in zone W than in zone E, as presented above. As a result, the three-core sandwich pattern is not clear or disappears (not complete) in the salinity anomaly related to eddies in zone W (Figs. 4c and 5c). This is in agreement with a two-layer structure of vertical salinity anomaly within composite eddies, described by Sun et al. (2018), in the SCS. The above differences in the salinity anomaly pattern are also seen in Fig. 6c, d.

3.2 Horizontal structure of eddy

At several representative levels, horizontal patterns of temperature, salinity, and geostrophic velocity anomalies within the composite eddies for each zone are plotted in Fig. 7. The patterns of temperature anomaly at the surface and at 10 dbar depth agree well with each other although they were obtained from independent data source and so do the patterns for geostrophic velocity anomaly. These indicate that at 10 dbar depth, the composite eddies based on Argo observations are reasonable.

Seen from geostrophic velocity anomaly (bottom panels in Fig. 7), circular currents related to eddies are very clear in both zone E and zone W. Their strength decreases with depth, and meanwhile, their range shrinks towards the eddy center, like a “bowl.” Here, the geostrophic velocity anomaly in Fig. 7 further confirms that the eddies in zone W are weaker in strength and have shallower influence depth than those in zone E, as discussed in the preceding subsection. In zone E, the velocity within the AE is stronger than that within the CE while their influence depths are almost the same (approximately 600 dbar). In zone W, the strength of velocity is weaker and the influence depth is shallower within the CE, compared with their counterparts within the AE. Statistic results from satellite SLA data also demonstrated that the AEs are stronger on average, with a larger mean surface geostrophic velocity, than the CEs in the northeast SCS (Guo et al. 2007).

Although circular streamlines can be found in the entire water column of the eddies, no closed contours of temperature and salinity anomalies are present around the eddy center in the layer above 100 dbar where a dipole structure rather than a single central core (monopole structure) appears (Fig. 7). This implies the primary effect of horizontal advection on the temperature and salinity distributions in the upper layer of eddies in the study region. Previous studies have demonstrated that the horizontal advection effect dominates in the formation of surface dipole structures of temperature and chlorophyll anomalies within eddies (e.g., Chelton et al. 2011; Chow and Liu 2013; Gaube et al. 2015). This effect depends on both eddy-induced current and the gradient of background field. In a field with a strong horizontal gradient of temperature/salinity, circular currents within an eddy transport warm/salty seawater from high temperature/salinity area to low temperature/salinity area, producing a positive anomaly in one side, and

meanwhile, they move cold/fresh seawater from low temperature/salinity area to high temperature/salinity area, generating a negative anomaly on the opposite side. As a result, a dipole structure occurs.

The advection effect on temperature can be estimated based on the flow field of the eddy and the mean gradient of background temperature (Chow and Liu 2012). Following Chow and Liu (2012), eddy-induced horizontal thermal advection (EHTA) at the surface was calculated by the following equation:

$$\text{EHTA} = -\mathbf{V}'_s \cdot \nabla \text{SST}_b = -u'_s \frac{\partial \text{SST}_b}{\partial x} - v'_s \frac{\partial \text{SST}_b}{\partial y}$$

where SST_b is the background temperature at the surface, namely climatological surface temperature as shown in Fig. 1b. Figure 8 shows the composite surface horizontal thermal advection within the CEs/AEs for each zone. In zone W west of the LS, the isotherms extend basically in the northeast–southwest direction and temperature increases from northwest to southeast (Fig. 1b). Thus, the thermal advection is positive in the northeastern half and negative in the southwestern half of the CE due to counterclockwise currents (Fig. 8a). The case is just the opposite for the AE because of clockwise currents (Fig. 8b). By contrast, the isotherms distribute roughly along the northwest–southeast direction and temperature increases from northeast to southwest in zone E (Fig. 1b). Positive thermal advection occurs in the eastern and northeastern parts, and negative one appears in the western and southwestern parts of the CE (Fig. 8c). For the AE in zone E, positive and negative advectations are in the northwestern and southeastern parts (Fig. 8d), respectively. The positive (negative) thermal advection tends to produce positive (negative) temperature anomaly. At the surface, the above dipole thermal advection patterns are consistent with the dipole temperature anomaly structures shown in Fig. 7. The horizontal advection has a similar effect on the salinity anomaly patterns within the eddies in zone W and zone E (see the middle row of Fig. 7), which depend on eddy-induced circular current and background salinity gradient.

In contrast to the horizontal advection, eddy pumping (upwelling within the CE and downwelling within the AE) usually generates a monopole structure of temperature/salinity anomaly around the eddy center. The dipole structure is often asymmetric due to the superposition of eddy-induced vertical advection effect, horizontal advection effect, and the effect related to eddy propagation (Chelton et al. 2011; Gaube et al. 2013, 2015). From the surface to the depths, the horizontal dipole structure of temperature anomaly turns gradually to a monopole structure (Fig. 7). This indicates that compared with the vertical advection

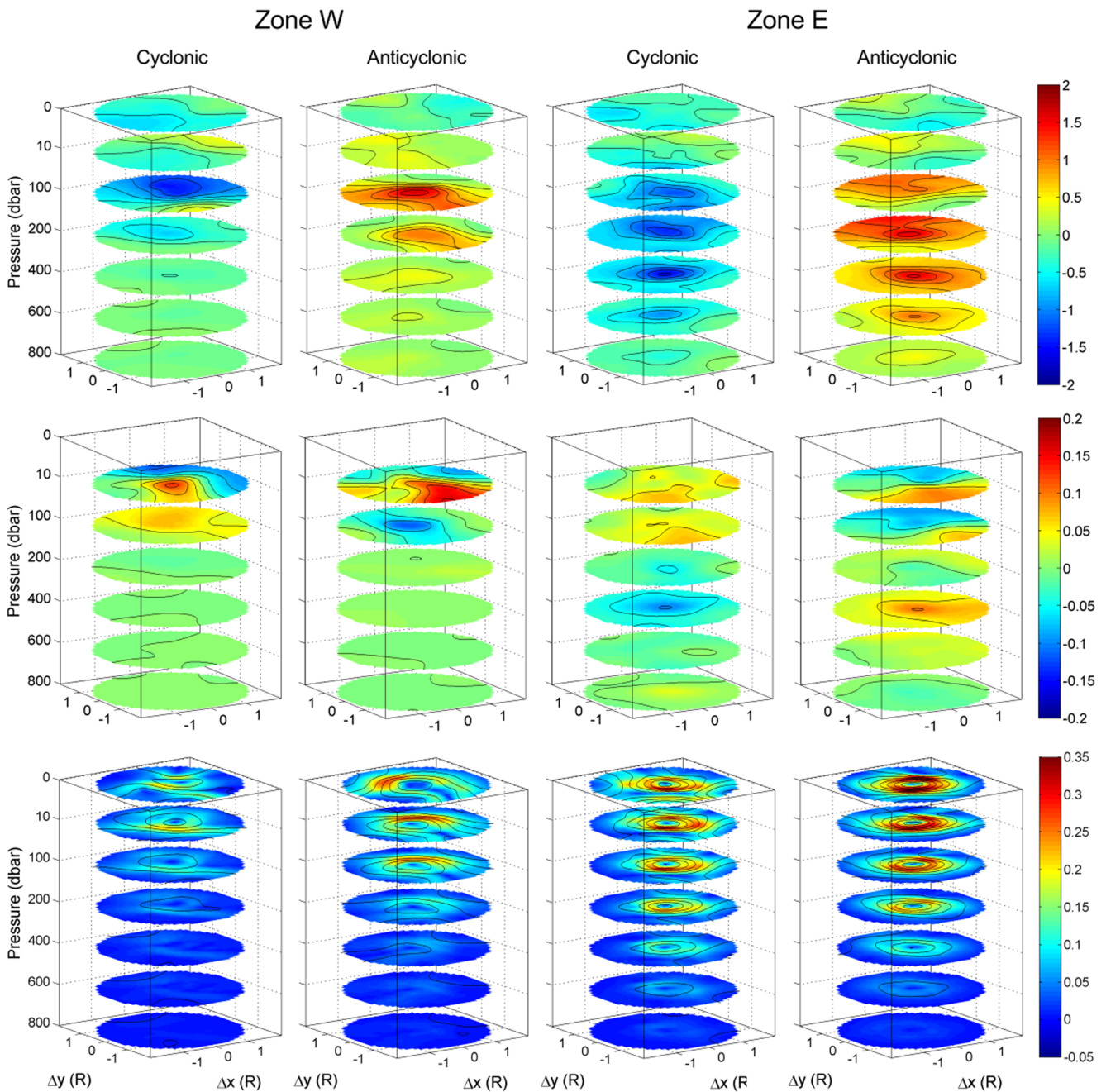


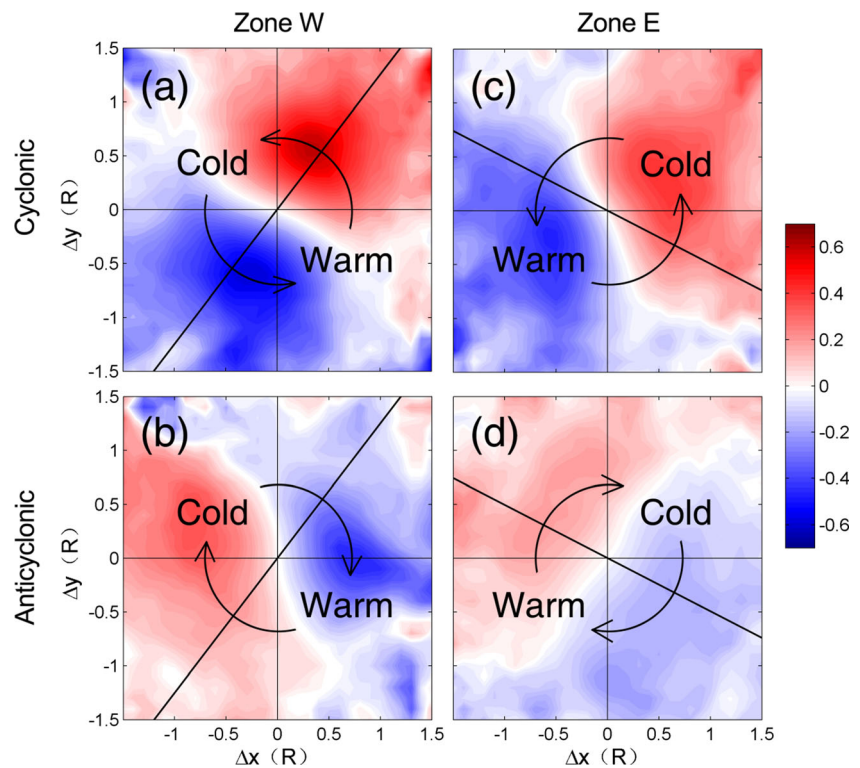
Fig. 7 Horizontal slices of θ' ($^{\circ}\text{C}$, top), S' (psu, middle), and geostrophic current speed anomaly V' (m/s, bottom) at 0, 10, 100, 200, 400, 600, and 800 dbar in the composite eddies of each zone. The contour interval is $0.25\text{ }^{\circ}\text{C}$ and 0.05 psu for θ' and S' , respectively. The contours of dynamic

height anomaly H' (m) with an interval of 0.02 m overlay the slices of V' . The surface θ' and V' are composited using the satellite SST and SLA observations at the same times and locations as the Argo profiles (see text for details)

effect, the horizontal advection gradually becomes insignificant (Fig. 7) when eddy-induced rotational current weakens with depth (Figs. 4e, f and 5e, f). In zone W, the dipole structure of temperature anomaly exists only in a shallow upper layer (above 30 dbar for the CE and 60 dbar for the AE), below which the horizontal structure has the characteristic of a central core with negative anomaly in the CE and positive anomaly in the AE. In zone E, such

a central core emerges at 70 dbar for the CE and at 130 dbar for the AE. Without considering the disturbance from eddy propagation (Gaube et al. 2015), the horizontal temperature anomaly structures within cyclonic and anticyclonic eddies in a field with a strong background temperature gradient are schematically explained in Fig. 9. In the upper layer, the temperature anomaly pattern is a dipole due to eddy-induced horizontal advection and it is asymmetric

Fig. 8 Compositions of surface horizontal thermal advection (shading, °C/week) due to eddy currents, based on 289 (166) CEs and 257 (162) AEs in zone E (zone W) as presented in Table 1. Thick solid lines roughly denote the orientation of background isotherms near the Kuroshio current, according to Fig. 1b. “Warm” and “cold” in each panel mean the high temperature area and low temperature area on both sides of the thick line, respectively. Arrows mark the directions of eddy-induced currents



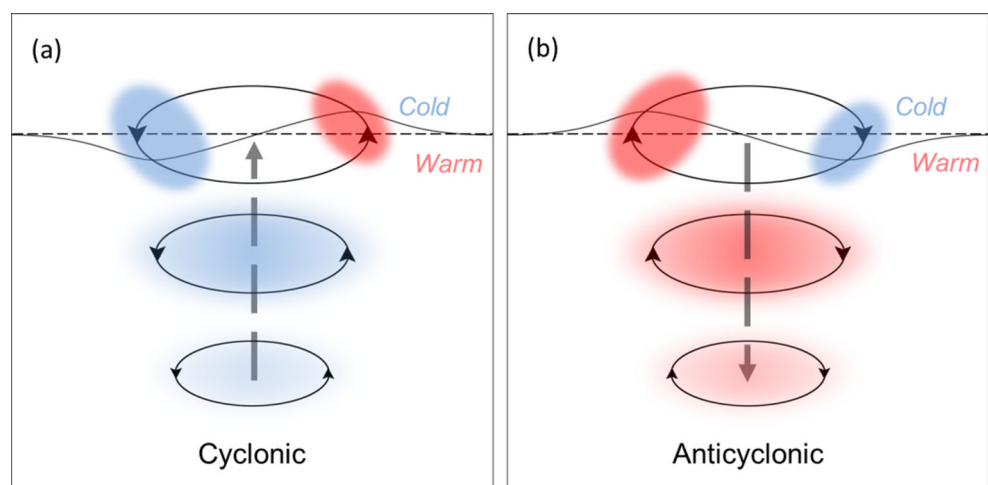
due to eddy pumping. In the deep layer, the pattern is a monopole with positive anomaly in an AE and negative anomaly in a CE.

3.3 Influence of the Kuroshio current

Generally, the salinity anomaly is negative in the surface layer of an AE due to prevailing downwelling in the eddy center, as that in zone E shown in Figs. 5d and 6d. However, it is noticed that in the core area of the composite AE in zone W, the salinity anomaly is clearly positive in the surface layer above 50 dbar (Figs. 5c and 6c). This indicates that high

salinity water in the surface layer of the AE in zone W has a different source, likely from the salty Kuroshio water. Previous studies have shown that many eddies in the northeastern SCS were shed from the Kuroshio and captured some salty Kuroshio water as they moved westward (e.g., Li et al. 1998; Jia and Chassignet 2011; Nan et al. 2015). During early September 1994, Li et al. (1998) observed an AE shedding from the Kuroshio in the northeastern SCS whose core had temperature and salinity properties between the Kuroshio water and the SCS water. Using altimetry data and outputs of the Hybrid Coordinate Ocean Model, Jia and Chassignet (2011) investigated the eddy shedding process from the

Fig. 9 Schematic diagram of the three-dimensional structure of eddy-induced thermal advection for **a** CEs and **b** AEs in the areas with large SST gradient. The red and blue patches correspond to positive and negative θ' , respectively. The horizontal advection of eddy currents leads to an asymmetric θ' dipole near the surface, whereas the vertical advection of upwelling/downwelling results in a θ' core at depths

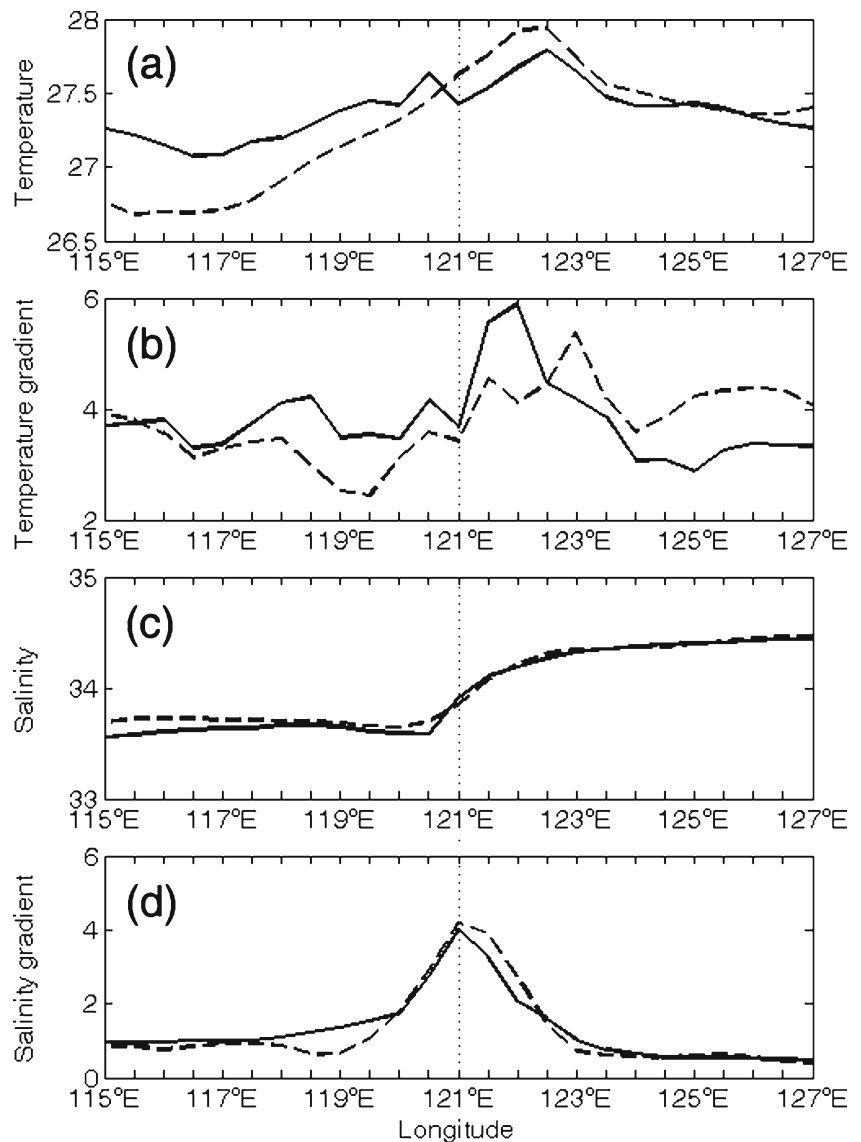


Kuroshio, suggesting that the Kuroshio intrudes into the northeastern SCS in a loop form; about a month later, a closed contour of sea surface height occurs inside the loop, and then an AE detaches from the Kuroshio intrusion. Actually, the eddy shedding process has been regarded as a type of the Kuroshio intrusion into the SCS (Hu et al. 2000; Nan et al. 2015). Entrained Kuroshio high-salinity water in many AEs shedding from the Kuroshio makes their surface layer water saltier than the surrounding SCS water when they move westward, resulting in the positive salinity anomaly in the surface layer of the composite AE in zone W.

As a northward-flowing current with high temperature across the LS, the Kuroshio influences the temperature distribution in the study region. An obvious warm tongue extends northward along the Kuroshio path, as shown in Fig. 1b. As a result, the isotherms west of the Kuroshio are arranged from the northeast to the southwest while those east of the Kuroshio

are from the northwest to the southeast. The distribution of the isotherms determines the orientation of the temperature dipole structure due to horizontal advection. This is the reason why the temperature anomaly patterns in zone W and zone E have a similar dipole structure at the surface but their orientations are very different (Fig. 8). Additionally, both meridionally averaged surface temperature in zones W and E and that in the zonal band through the LS between two horizontal dashed lines marked in Fig. 1b show that the temperature in the path of the Kuroshio current is obviously higher than those of its west and east flanks (Fig. 10a). This produces a stronger temperature gradient to the right of 121° E, just east of the LS (Fig. 10b). The LS where the Kuroshio flows by is the transitional region from the Pacific water with higher salinity to the SCS water with lower salinity (Fig. 10c). A significant peak of meridionally averaged surface salinity gradient occurs here (Fig. 10d). The enhanced temperature and salinity gradients

Fig. 10 Meridional mean values of **a** temperature (°C), **b** temperature gradient magnitude (10^{-6} °C/m), **c** salinity (psu), and **d** salinity gradient magnitude (10^{-6} psu/m) at the surface, based on climatological data. Solid curves denote the results in zone W and zone E, and dashed curves denote the results obtained in the area between the two horizontal dashed lines shown in Fig. 1b



are partly responsible for the great horizontal advection effect on the temperature and salinity structures in the upper layer of eddies on both sides of the LS. We similarly reconstructed the composite AE and CE in an area (130°–135° E, 16°–25° N) far away from the Kuroshio current, but the dipole patterns of temperature and salinity anomalies in the upper layer of these eddies are not as significant as those in zone E (figure omitted).

4 Summary

Based on Argo observations and satellite remote sensing data during the period of 2002–2014, the mean 3D structures in temperature, salinity, and velocity anomalies of eddies on both sides of the LS were obtained via a composite method and analyzed to statistically examine the influence of background marine environment and the Kuroshio current on the eddy structures. The composite structures of eddies show evident differences between zone E east of the LS and zone W west of the LS due to different eddy intensity, background marine environment, and influence of the Kuroshio current.

Compared with eddies in zone W, eddies in zone E are obviously stronger based on their amplitude, radius, and circular current. The significant signals of temperature and salinity anomalies within the composite eddies extend much deeper in zone E than those in zone W because of stronger eddy intensity and larger vertical gradients of background temperature and salinity in the deep layer in zone E. Two cores occur at around 200 and 400 dbar depths, respectively, in the vertical structure of temperature anomaly inside the eddies in zone E due to the existence of the STMW. Only one core centered at about 100 dbar is present inside the eddies in zone W since there is no STMW. There is a clear three-core sandwich pattern in the vertical structure of salinity anomaly within the eddies in zone E while the three-core pattern is not clear in zone W. In zone W, salinity anomaly in the surface layer of the AE center is clearly positive, rather than negative that is commonly found in the AE, indicating the Kuroshio water trapped in the eddy.

Horizontal structures of temperature and salinity anomalies in eddies depend on the competition between horizontal advection effect and eddy pumping effect. On both sides of the LS, an asymmetric dipole structure in the surface layer gradually turns into a monopole one at depths because the horizontal advection effect decreases with depth. The Kuroshio current flowing northward across the LS arranges the isotherms and isohalines and enhances background temperature and salinity horizontal gradients in the upper layer on the two sides of the LS, which determines the orientations of dipole structures of temperature and salinity anomalies within eddies in the study region. In zone W (zone E), the dipole

temperature structure trends to align in the northeast–southwest (northwest–southeast) direction.

In the statistical sense, the composite eddies presented in this study showcase the 3D structures and the differences for eddies from either side of the LS. The Kuroshio current definitely affects the eddy structures on both sides of the LS. These results lay a basic and observational foundation for future modelling studies in this region.

Acknowledgments This study is a contribution to the international IMBER project. The daily SLA data were provided by the AVISO data project, and the daily satellite AVHRR SST data were obtained from the National Climatic Data Center (NCDC) of the National Oceanic and Atmospheric Administration (NOAA). The Argo float profiles were downloaded from the China Argo Real-time Data Center, and the Argo-only version of CARS was from the CSIRO (<http://www.marine.csiro.au/atlas/>).

Funding information This work was jointly funded by the State Key R&D project (grant no. 2016YFA0601103), the National Natural Science Foundation of China (grants 41776015 and 41276007), and President Research Award (2013121047).

References

- Akima H (1970) A new method of interpolation and smooth curve fitting based on local procedures. *J ACM (JACM)* 17:589–602
- Aoki S, Imawaki S (1996) Eddy activities of the surface layer in the Western North Pacific detected by satellite altimeter and radiometer. *J Oceanogr* 52:457–474
- Barth A, Beckers JM, Troupin C, Alvera-Azcárate A, Vandenbulcke L (2014) divand-1.0: n-dimensional variational data analysis for ocean observations. *Geosci Model Dev* 7:225–241
- Caruso MJ, Gawarkiewicz GG, Beardsley RC (2006) Interannual variability of the Kuroshio intrusion in the South China Sea. *J Oceanogr* 62:559–575
- Chaigneau A, Gizolme A, Grados C (2008) Mesoscale eddies off Peru in altimeter records: identification algorithms and eddy spatio-temporal patterns. *Prog Oceanogr* 79:106–119
- Chaigneau A, Eldin G, Dewitte B (2009) Eddy activity in the four major upwelling systems from satellite altimetry (1992–2007). *Prog Oceanogr* 83:117–123
- Chaigneau A, Le Texier M, Eldin G, Grados C, Pizarro O (2011) Vertical structure of mesoscale eddies in the eastern South Pacific Ocean: a composite analysis from altimetry and Argo profiling floats. *J Geophys Res* 116:C11025
- Chelton DB, Gaube P, Schlax MG, Early JJ, Samelson RM (2011) The influence of nonlinear mesoscale eddies on near-surface oceanic chlorophyll. *Science* 334:328–332
- Chen G, Hou Y, Chu X (2011) Mesoscale eddies in the South China Sea: mean properties, spatiotemporal variability, and impact on thermohaline structure. *J Geophys Res* 116:C05021
- Chow CH, Liu Q (2012) Eddy effects on sea surface temperature and sea surface wind in the continental slope region of the northern South China Sea. *Geophys Res Lett* 39:L02601
- Chow CH, Liu Q (2013) Eddy-advective effects on the temperature and wind speed of the sea surface in the Northwest Pacific Subtropical Countercurrent area from satellite observations. *Int J Remote Sens* 34:600–612

- Chu X, Xue H, Qi Y, Chen G, Mao Q, Wang D, Chai F (2014) An exceptional anticyclonic eddy in the South China Sea in 2010. *J Geophys Res* 119:881–897
- Gaube P, Chelton DB, Strutton PG, Behrenfeld MJ (2013) Satellite observations of chlorophyll, phytoplankton biomass, and Ekman pumping in nonlinear mesoscale eddies. *J Geophys Res* 118:6349–6370
- Gaube P, Chelton DB, Samelson RM, Schlax MG, O'Neill LW (2015) Satellite observations of mesoscale eddy-induced Ekman pumping. *J Phys Oceanogr* 45:104–132
- Guo J, Yuan Y, Xiong X, Guo B (2007) Statistics of the mesoscale eddies on both sides of the Luzon Strait. *Advances in Marine Science* 25(2):139–148 (in Chinese with English abstract)
- Hu J, Kawamura H, Hong H, Qi Y (2000) A review on the currents in the South China Sea: seasonal circulation, South China Sea warm current and Kuroshio intrusion. *J Oceanogr* 56:607–624
- Jia Y, Chassignet EP (2011) Seasonal variation of eddy shedding from the Kuroshio intrusion in the Luzon Strait. *J Oceanogr* 67:601–611
- Li L, Nowlin WD Jr, Su J (1998) Anticyclonic rings from the Kuroshio in the South China Sea. *Deep Sea Res Part I: Oceanographic Res Papers* 45:1469–1482
- Li J, Zhang R, Jin B (2011) Eddy characteristics in the northern South China Sea as inferred from Lagrangian drifter data. *Ocean Sci* 7:661–669
- Lin X, Dong C, Chen D, Liu Y, Yang J, Zou B, Guan Y (2015) Three-dimensional properties of mesoscale eddies in the South China Sea based on eddy-resolving model output. *Deep Sea Res Part I: Oceanographic Res Papers* 99:46–64
- Liu Y, Dong C, Guan Y, Chen D, McWilliams J, Nencioli F (2012) Eddy analysis in the subtropical zonal band of the North Pacific Ocean. *Deep Sea Res Part I: Oceanographic Res Papers* 68:54–67
- Nan F, Xue H, Yu F (2015) Kuroshio intrusion into the South China Sea: a review. *Prog Oceanogr* 137:314–333
- Nencioli F, Dong C, Dickey T, Washburn L, McWilliams JC (2010) A vector geometry-based eddy detection algorithm and its application to a high-resolution numerical model product and high-frequency radar surface velocities in the southern California Bight. *J Atmos Ocean Technol* 27:564–579
- Qu T, Mitsudera H, Yamagata T (2000) Intrusion of the North Pacific waters into the South China Sea. *J Geophys Res* 105:6415–6424
- Roemmich D, Gilson J (2001) Eddy transport of heat and thermocline waters in the North Pacific: a key to interannual/decadal climate variability? *J Phys Oceanogr* 31:675–687
- Souza JMAC, de Boyer MC, Cabanes C, Klein P (2011a) Estimation of the Agulhas ring impacts on meridional heat fluxes and transport using ARGO floats and satellite data. *Geophys Res Lett* 38:L21602
- Souza JMAC, de Boyer MC, Le Traon PY (2011b) Comparison between three implementations of automatic identification algorithms for the quantification and characterization of mesoscale eddies in the South Atlantic Ocean. *Ocean Sci* 7:317–334
- Suga T, Hanawa K (1995) The subtropical mode water circulation in the North Pacific. *J Phys Oceanogr* 25:958–970
- Sun W, Dong C, Wang R, Liu Y, Yu K (2017) Vertical structure anomalies of oceanic eddies in the Kuroshio Extension region. *J Geophys Res Oceans* 122:1476–1496
- Sun W, Dong C, Tan W, Liu Y, He Y, Wang J (2018) Vertical structure anomalies of oceanic eddies and eddy-induced transports in the South China Sea. *Remote Sens* 10(795):1–24
- Wang G, Su J, Chu PC (2003) Mesoscale eddies in the South China Sea observed with altimeter data. *Geophys Res Lett* 30(21):2121
- Wang L, Kobalinsky CJ, Howden S (2000) Mesoscale variability in the South China Sea from the TOPEX/Poseidon altimetry data. *Deep Sea Res Part I: Oceanographic Res Papers* 47:681–708
- Wang G, Chen D, Su J (2008) Winter eddy genesis in the eastern South China Sea due to orographic wind jets. *J Phys Oceanogr* 38:726–732
- Wang X, Li W, Qi Y, Han G (2012) Heat, salt and volume transports by eddies in the vicinity of the Luzon Strait. *Deep Sea Res Part I: Oceanographic Res Papers* 61:21–33
- Xiu P, Chai F, Shi L, Xue H, Chao Y (2010) A census of eddy activities in the South China Sea during 1993–2007. *J Geophys Res* 115:C03012
- Yang G, Wang F, Li Y, Lin P (2013) Mesoscale eddies in the northwestern subtropical Pacific Ocean: statistical characteristics and three-dimensional structures. *J Geophys Res* 118:1906–1925
- Zhang Z, Zhang Y, Wang W, Huang RX (2013) Universal structure of mesoscale eddies in the ocean. *Geophys Res Lett* 40:3677–3681
- Zhang W-Z, Xue H, Chai F, Ni Q (2015) Dynamical processes within an anticyclonic eddy revealed from Argo floats. *Geophys Res Lett* 42:2342–2350
- Zhang Z, Tian J, Qiu B, Zhao W, Chang P, Wu D, Wan X (2016) Observed 3D structure, generation, and dissipation of oceanic mesoscale eddies in the South China Sea. *Sci Rep* 6:24349